Journal of Applied Physics

RESEARCH ARTICLE | JULY 24 2024

Efficient characterization of a double quantum dot using the Hubbard model

Will Wang ; John Dean Rooney ; Hongwen Jiang

J. Appl. Phys. 136, 044401 (2024)
https://doi.org/10.1063/5.0215622

AIP Publishing

Journal of Applied Physics ARTICLE pubs.aip.org/aip/jap

Efficient characterization of a double quantum dot using the Hubbard model

Cite as: J. Appl. Phys. **136**, 044401 (2024); doi: 10.1063/5.0215622
Submitted: 25 April 2024 · Accepted: 25 June 2024 ·
Published Online: 24 July 2024

Will Wang,[a] John Dean Rooney, and Hongwen Jiang

AFFILIATIONS

Department of Physics and Astronomy, University of California, Los Angeles, California 90095, USA

[a]**Author to whom correspondence should be addressed:** qinghe1230@ucla.edu

ABSTRACT

Semiconductor quantum dots are favorable candidates for quantum information processing due to their long coherence time and potential scalability. However, the calibration and characterization of interconnected quantum dot arrays have proven to be challenging tasks. One method to characterize the configuration of such an array involves using the Hubbard model. In this paper, we present an efficient characterization algorithm that efficiently extracts the Hubbard model parameters, including tunnel coupling and capacitive coupling energy, from experimental stability diagrams. Leveraging the dual-annealing optimizer, we determine the set of Hubbard parameters that best characterize the experimental data. We compare our method with an alternate, well-established measure of tunnel coupling and find good agreement within the investigated regime. Our extracted tunnel couplings range from 69 to 517 μeV, and we discuss the limiting factors of our method.

I. INTRODUCTION

Semiconductor quantum dots are among the most promising hardware platforms for quantum information processing. In recent years, both single and two-qubit operations using electron spins have been carried out with fidelities above 99%.[1] Electron spins in silicon also have a long coherence time, making them robust to decoherence effects observed in other solid state systems.[2] Furthermore, the fabrication of these devices can be easily integrated with the classical semiconductor industry, making semiconductor qubit a true candidate for scalable quantum computing.

However, calibrating a quantum dot array to a desired working point has proven to be nontrivial, due to the large parameter space and each quantum dot having unique parameters compared to its neighbors. This makes the characterization of these devices especially important. To achieve single and two-qubit operations in a quantum dot array, it is imperative to know the tunnel coupling between two neighboring quantum dots. Furthermore, recent works had demonstrated the possibility of simulating the Hubbard model with a quantum dot array.[3,4] To achieve a direct mapping between a quantum dot array and the Hubbard model, it is also essential to know the values of the Hubbard model parameters at a given voltage configuration.

One of the primary distinctions of the Hubbard model from the capacitive model is the account of tunnel coupling between neighboring sites. Conventionally, the tunnel coupling energy is extracted from the expectation value of the double dot charge polarization averaged over a Maxwell–Boltzmann distribution.[5–7] This measurement, which we will henceforth label the DiCarlo method, is performed by measuring the electron temperature and the polarization linewidth at the desired anti-crossing in stability diagrams. To obtain an accurate measurement, additional experimental setups are required for measuring the electron temperature; furthermore, adjustments to the lock-in voltage are needed to bring out the anti-crossing polarization line on the stability diagram. Additionally, at the limit of extremely large tunnel coupling, this method becomes difficult to perform due to the extensive broadening of the polarization line.

Another parameter in the Hubbard model that is crucial for studying the coupling between neighboring quantum dots is the capacitive coupling energy. It has been shown that this coupling energy can be directly obtained by measuring the length of the anti-crossing while converting from voltage to energy space with the appropriate lever arms.[8] However, this method is limited to the low-tunnel-coupling region where the tunnel effect remains small.

The addition of tunnel coupling distorts and increases the spacing of the anti-crossings, making the isolation of the capacitive coupling energy difficult through this simple measurement.[9]

Inspired by the works of Sarma *et al.*, we developed a novel method that efficiently extracts the Hubbard model parameters directly from experimental stability diagrams.[9–11] As discussed in Ref. 10, information regarding the Hubbard model is contained in the geometry of the stability diagrams.[34] Building on this work, we study the possibility of extracting the Hubbard parameters directly from experimentally obtained stability diagrams with depth and compare our results, specifically the tunnel coupling measurement, to the DiCarlo method. We have found an agreement with the DiCarlo method; however, we will also discuss the limitations of our method. We demonstrate our method's ability to extract the capacitive coupling energy in the large tunnel coupling limit, which has yet to be done solely from the geometry of the stability diagram.

We acknowledge that there has been previous work done on characterizing and calibrating the state of a quantum dot array including the measurements of either tunnel coupling or capacitive coupling energy. For instance, in an earlier work, the authors proposed an automated procedure for tuning the tunnel coupling,[12] while in another work, the authors discussed tuning the tunnel coupling of a quantum dot array.[13] However, both papers are different from our approach, where we obtained the tunnel coupling directly from the curvatures of the polarization lines. Additionally, although the former mentions fitting the anti-crossing, their fitting is fundamentally different from our approach, which involves the Hubbard model.[12] In another work, an automated tuning protocol was proposed.[14] While this method differentiates tunnel coupling with the curvatures of the anti-crossings, its measurements are purely qualitative and are unable to identify the exact tunnel coupling value. Two previous works both used a two-site Hubbard model to model a specific anti-crossing; however, quantitative measurements of the tunnel coupling were not reported from fitting the anti-crossing geometry.[15,16] In particular, the latter used a two-site Hubbard model to extract the exact location of the triple points; however, the exact tunnel coupling was measured from the broadening of the inter-dot transition line.[16] Similar to the works mentioned above, there have been multiple previous works on the subject; however, these works have not quantitatively measured the inter-dot tunnel coupling or the capacitive coupling in the large tunnel coupling regime; furthermore, their measurements of the tunnel coupling utilize the broadening of the inter-dot transition line, photon-assisted tunneling, or time-resolved charge sensing, differing from our approach that solely leverages the geometry of the stability diagrams.[8,17–31]

II. BACKGROUND

A. Experimental setup

For this paper, we used a device (Fig. 1) with two quantum dots and an adjacent quantum point contact (QPC), which are defined by gate electrodes fabricated on top of a Si/SiGe heterostructure. The two-dimensional electron gas was formed by a positive voltage applied to a global top gate located above the gate electrodes and insulated by a 100 nm layer of aluminum oxide. Note that the measurements in this paper were performed only with the two lower dots of the device, while the upper portion was left completely open. The two lower dots are coupled by barrier gate

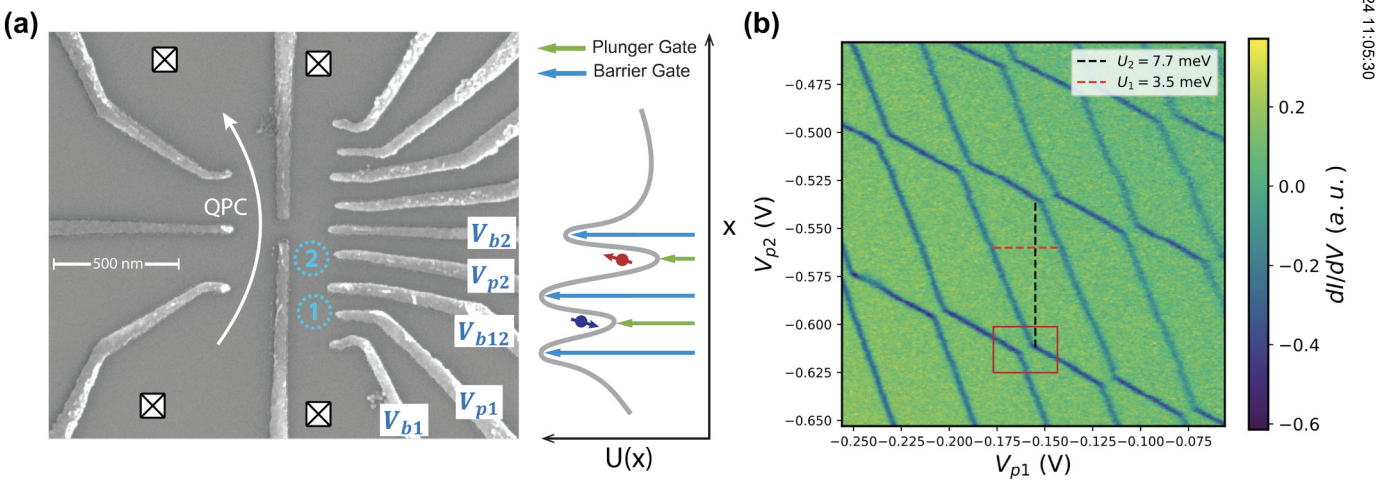

FIG. 1. (a) (Left) SEM diagram of the quantum dot array that was used to perform the measurements in this work. The two blue dotted circles are approximately the positions of the quantum dots, and the QPC is labeled on the left-hand side of the device. (Right) A two-site Hubbard model illustration: the gray line depicts the potential landscape of the two dots. The blue and green arrows underneath represent the effects of plunger and barrier gates. In the Hubbard model, plunger gates would be directly related to the chemical potential of each dot; and the barrier gate is used to tune the coupling energy as well as the tunnel coupling. Conceptually, the charging energies of the dots correspond to the size of the dots. (b) A large stability diagram in the low-tunneling regime containing multiple anti-crossings. The dark pixels indicate a rapid change in the current of the QPC. We pick the anti-crossing in the red square as the one to be investigated (this choice is arbitrary). Note that the color bar will be omitted for the rest of the paper. The charging energies for each dot can be directly measured as the distance between horizontal (red, QD1) and vertical (black, QD2) transition lines. The cross-capacitances can be measured from the slopes of the transition lines.

V_{b12}. The QPC gates are tuned such that the current flowing through the left channel is sensitive to electron transport in the two dots.

The chemical potential of dot 1(2) was primarily controlled through plunger 1(2) above the dot (denoted as $V_{p1(2)}$). By tuning the plunger voltages, electrons can hop on and off the dots from the source and drain reservoirs and in between each dot. Electron tunneling was detected as a change in the transconductance signal measured by a lock-in connected to the QPC, while the lock-in's excitation voltage was applied to both plungers. As shown in Fig. 1(b), electron transport in a double quantum dot can be well visualized with stability diagrams created from pairwise scanning of neighboring plungers.

To determine each plunger's lever arm, we followed the procedure in Ref. 6. We measured the full width at half maximum (FWHM) of the polarization linewidths for both dots as a function of fridge temperature T_f. For high T_f, the polarization line's FWHM becomes proportional to T_f, allowing lever arms to be extracted from the proportionality constant. The extracted lever arms values are 0.1 ± 0.02 eV/V for both plunger gates to their respective dots.

B. The Hubbard model

Conventionally, it is common to model the dynamics of a quantum dot array with the capacitive model.[32] While this model captures the effects of Coulomb blockade and the capacitive coupling between coupled quantum dots, it fails to account for the quantum fluctuation. In order to incorporate the quantum effects in our models, we need to use the extended Hubbard model, a model often used to describe interacting particles on a lattice. To apply the extended Hubbard model to a quantum dot array, we use the following Hamiltonian:[9]

$$\hat{\mathcal{H}} = -\sum_i \mu_i \hat{n}_i - \sum_{\langle i,j\rangle,\sigma} t_{ij}\left(\hat{c}^\dagger_{i\sigma}\hat{c}_{j\sigma} + \hat{c}^\dagger_{j\sigma}\hat{c}_{i\sigma}\right) + \sum_i \frac{U_i}{2}\hat{n}_i(\hat{n}_i - 1) + \sum_{i\neq j} U_{ij}\hat{n}_i\hat{n}_j, \quad (1)$$

where $\hat{c}_{i\sigma}$ and $\hat{c}^\dagger_{i\sigma}$ are the fermionic creation and annihilation operators at site i with spin σ (either $\uparrow$ or $\downarrow$); the number operator is defined as $\hat{n}_{i\sigma} = \hat{c}^\dagger_{i\sigma}\hat{c}_{i\sigma}$; ϵ is the single-particle energy offset; t_{ij} is the tunnel coupling between dots i and j; U_i is the charging energy on dot i; U_{ij} is the capacitive coupling energy between dot i and j; and finally, $\langle i, j\rangle$ denotes neighboring sites i and j. Putting things in a broader context—the first term in the Hamiltonian refers to the single-particle energy offsets; the second term is the hopping term that describes the tunneling effects between neighboring dots; the third term accounts for the on-site Coulomb interaction; and the last term is the inter-site Coulomb interaction. Note that the Hubbard model at the limit of zero tunnel coupling is completely equivalent to the capacitive model.[10] Also note that in the generic Hubbard model, there are terms that describe the effects of spin exchange, co-tunneling, etc.; however, we will discard these extra terms as their effects are insignificant in our experiment.

Generating stability diagrams from the Hubbard model is discussed in supplementary material I. In this work, we also developed a few techniques to speed up the simulation, which are discussed in supplementary material III.

III. METHOD

In this section, we will discuss the characterization protocols we have developed as well as the details of the optimization, including a discussion on optimizers.

A. Characterization procedures

Here, we provide a brief overview of the entire characterization procedure. We start with generating a large stability diagram in the low-tunneling regime and choose a specific anti-crossing as shown in Fig. 1(b).

We then measure the vertical and horizontal spacings between the transition lines to obtain the charging energies at low-tunnel coupling. These measurements are taken in the voltage space and are converted to energy units with the appropriate lever arms. For our devices, the lever arms are approximately $0.1\,\text{eV/V} = 100\,\text{meV/V}$. The measured charging energies for dots 1 and 2 are 3.5 and 7.7 meV, respectively.

In these devices, cross-capacitances contribute to the slopes of the transition lines. Therefore, we can also measure the cross-capacitances α, β of the two plunger gates from the slopes of the transition lines in the figure above.[33] Here, we find the cross-capacitances of dots 1 and 2 with respect to plunger gate V_{p2} and V_{p1} to be 0.56 and 0.42, respectively. Using the cross-capacitances, the relations between the raw voltage values and the chemical potentials are defined in Eqs. (1) and (2) in the supplementary material.

Since the cross-capacitance and the charging energy can be easily obtained from features in the stability diagram, such as the slope and distance between charging lines, we will keep them as fixed variables in the optimization. A two-dot Hubbard model consists of eight free parameters, including two charging energies, two cross-capacitances, two voltage offsets, the tunnel coupling, and the capacitive coupling energy. For the rest of the characterization, we will determine the four remaining parameters, that is, the capacitive and tunnel coupling, and the two voltage offsets.

Before the optimization, we first zoom into the target anti-crossing and perform scans with higher resolution at various barrier voltages. Specifically, we vary the barrier voltage from 0.1 to 0.24 V. All diagrams are taken at 125×125 resolution across 0.06 (V_{p2}) and 0.1 (V_{p1}) meV. These diagrams are shown in Fig. 2. From these plots, we see an increase in the line curvature as we increase the barrier gate voltage, suggesting an increase in tunnel coupling—consistent with what theory predicts.[9]

The rest of the characterization includes an optimization process that iteratively compares a simulated stability diagram and the target stability diagram. The entire optimization procedure is depicted in Fig. 3.

We start with an experimental stability diagram. After performing a set of thresholding and denoising, we arrive at a binary graph without the extra features. We first generate a simulated stability diagram in the same window from a set of guess Hubbard parameters. We then compare the simulated graph with the target graph with a cost function that characterizes the difference between the two diagrams. With the cost function defined, we can then

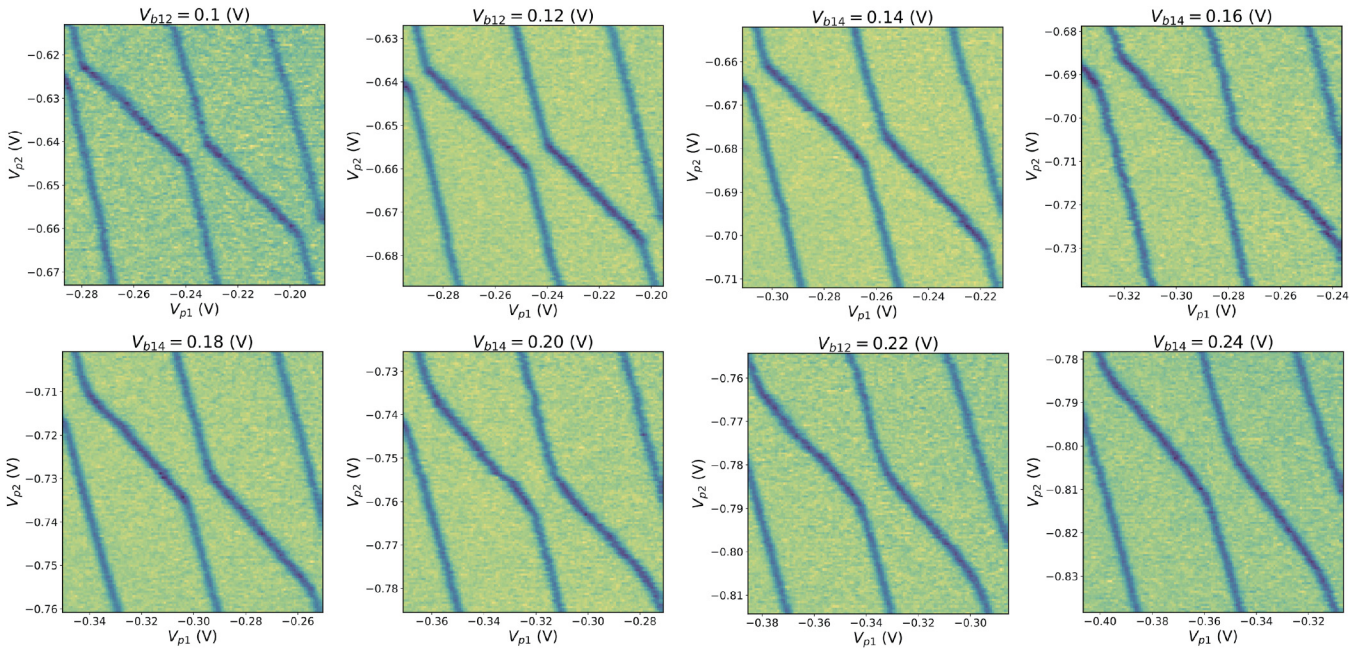

FIG. 2. Anti-crossings with barrier voltage values from 0.1 to 0.24 V. The window of the scan is adjusted so that every anti-crossing is roughly at the center of the scan. The curvatures of the anti-crossings are visibly increasing with increasing barrier gate voltage.

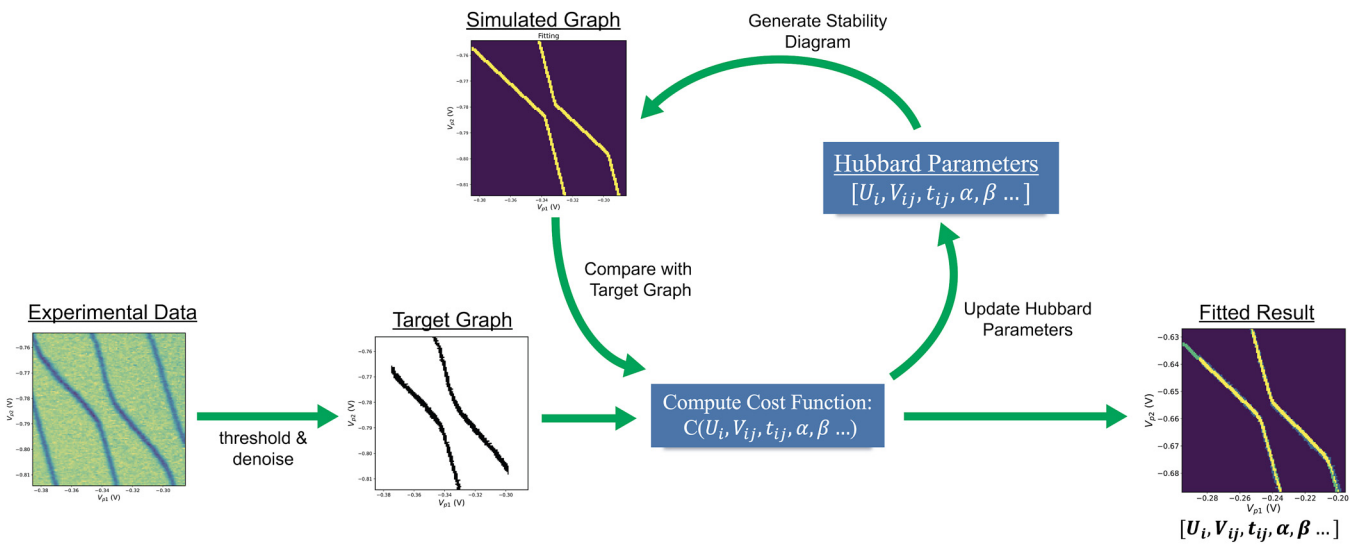

FIG. 3. Optimization demonstration. Starting from the experimental stability diagram, we first perform some thresholding and denoising to remove the unnecessary features in the stability diagram (including extra lines and corrupted regions). We also convert the z axis values into binary values. Starting from a set of guess Hubbard parameters, we produce a simulated stability diagram in the same window and calculate a cost function that characterizes the difference between the simulated and target diagram. We then optimize the Hubbard parameters with the dual-annealing optimizer until the optimization converges. On the right, we plot the simulated diagram with the optimal parameters over the target diagram.

perform a closed loop optimization to find the optimal value. We choose dual-annealing as the optimizer, since it has proven to be effective in escaping local minima (something we have encountered frequently). Last, a set of optimized Hubbard parameters is outputted after the optimization converges.

In this work, we studied an anti-crossing in the multi-electron regime (six to ten electrons) to minimize the effects of spin-exchange that are more visible in the (2,0)–(1,1) transition. Furthermore, we assume that the charging transition in the multi-electron regime can be described by an effective two-electron model, mapping to the (2,0)–(1,1) transition (analogous to an artificial atom with two valence electrons). As Sarma *et al.* argued in Ref. 10, a fully accurate calculation would require a multielectron and multiband calculation, which would be very time-consuming and is currently out of the scope of this work. Building upon the method developed in this work, we believe that incorporating a multiband calculation and studying the effects of the actual electron occupation numbers would be a very interesting extension.

IV. RESULT

In this section, we present the results of the characterization. We perform the fitting on all eight plots in Fig. 2 with different barrier gate voltages. The fitted results are displayed in Fig. 4.

From these plots, we see good correspondence between the simulation and the experimental data. For these fittings, we assume that the cross-capacitances and the charging energies remain constant as we increase the barrier voltage, which proved to be a reasonable assumption for the regime where we performed the fitting.

We plot the measured capacitive couplings (or coupling energies) and the tunnel couplings in Fig. 5. We observed that the coupling energies roughly remain constant in the measured region, while the tunnel coupling increases exponentially as the barrier voltage increases. In Fig. 5(a), we plot the measured tunnel couplings from our method to the tunnel couplings measured from the DiCarlo method. We found that our results agree well with the DiCarlo method, confirming the accuracy of this method. At the time of writing this paper, since there were no known methods for reliably measuring the capacitive coupling at the high tunnel coupling regime, we could not verify our electrostatic/capacitive coupling results with another known method.

We acknowledge that estimating the errors of the fitted parameters is nontrivial, since an analytical solution does not exist for such a system. For the scope of this experiment, we consider the error as a result of the error in measuring lever arms. We have numerically verified that the 20% error in lever arms results in 20% errors in all fitted parameters. The error in the DiCarlo method is estimated from the error in FWHM from the Gaussian fitting of polarization linewidth. A large discrepancy in the tunnel couplings between the DiCarlo method and our method is observed at $V_{b12} = 0.18\,\mathrm{V}$, and we attribute this discrepancy to improper thresholding and noise inherent in the measurement.

It is important to note that there are a few limiting factors to this method. In previous experiments, we have found degeneracies while fitting many parameters, in particular, the cross-capacitances

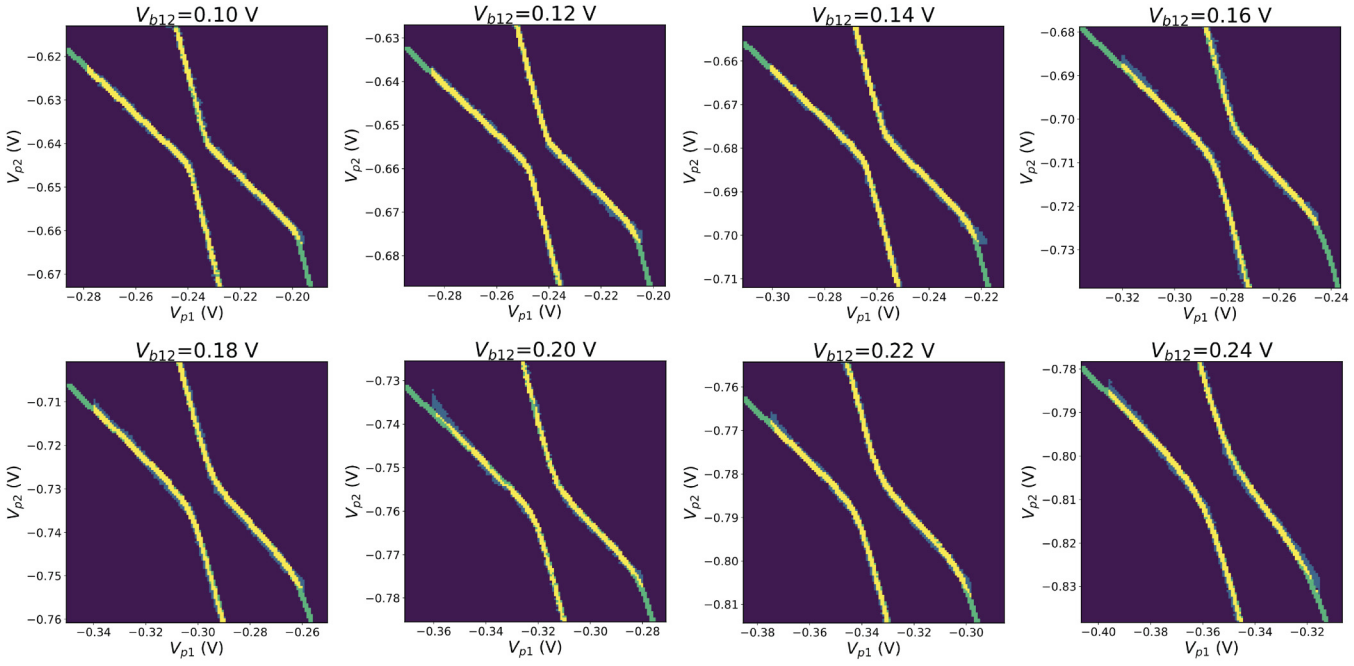

FIG. 4. Fitted results of anti-crossings with various barrier gate voltages. The simulated result is plotted on top of the experimental data. Green corresponds to the simulated stability diagram; blue corresponds to the experimental data; and yellow is the overlap between the two.

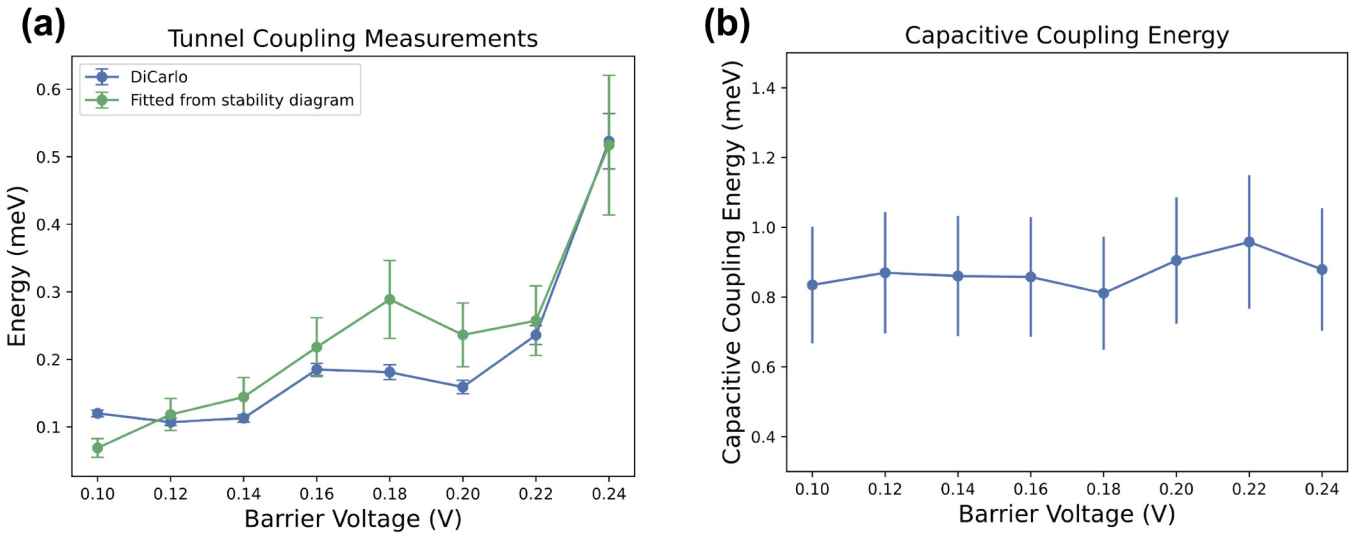

FIG. 5. Results from the Hubbard model characterization. (a) Measured tunnel couplings (green) comparison with the DiCarlo method (blue). (b) Measured capacitive couplings with respect to various barrier voltages.

and tunnel coupling. As the tunnel coupling is increased, the slopes of the transition lines between anti-crossings are corrupted by the increasing curvature; however, the cross-capacitances could "compensate" this effect during optimization and lead to inaccurate results. We note that this compensation effect also applies to the low-tunnel-coupling regime. However, since the quantum effects are relatively small in the low-tunneling regime, we expect the extracted cross-capacitances and charging energies to be accurate. Therefore, we measured the cross-capacitances and charging energies at the low-tunnel coupling regime and fixed their values during the optimization. As a result, this method would not be reliable if the cross-capacitance/charging energies vary much from the low-tunnel coupling regime.

Other factors include the polarization linewidth and stability diagram resolutions. While we found that these factors have minor effects on the results, they are not as impactful to the results as the degeneracy we have discussed previously.

V. CONCLUSION

In this work, we have developed an optimization protocol that extracts the Hubbard model parameters from the geometric features of experimental stability diagrams. Our method is able to measure large tunnel couplings, where the DiCarlo method is difficult to execute. We also demonstrated our method's ability to measure the capacitive coupling in this regime, which was only previously measured in the low-tunnel-coupling limit. This work allows for future studies on the relationship of the coupling between quantum dots and the barrier voltages that define their potential landscape. Furthermore, this model-based fitting approach also enables fine-tuning of the Hubbard model simulation using quantum dot arrays. We also note that this method has shown robustness to experimental noise/limitations such as missing pixels, wide polarization lines, and low pixel resolutions.

Some future work includes studying whether one could extract information regarding additional terms in the generic Hubbard model, such as the spin-exchange and pair-hopping terms. Last, we believe that this work can be easily generalized to a many-dot array and shows promise for high automation in the future, which is essential for the automated calibration of large quantum dot arrays.

SUPPLEMENTARY MATERIAL

Details regarding the Hubbard model simulations are included in the supplementary material. The supplementary material also includes various methods we developed to speed up the simulation and the cost function definition.

ACKNOWLEDGMENTS

The authors would like to acknowledge the Lisa Edge of HRL Laboratories for providing the Si/SiGe heterostructures. The authors also acknowledge the helpful discussion with Portia Wang on the line-tracing algorithm. The work was supported by ARO through Grant No. W911NF-23-1-0016.

AUTHOR DECLARATIONS

Conflict of Interest

The authors have no conflicts to disclose.

Author Contributions

Will Wang: Conceptualization (equal); Data curation (lead); Investigation (lead); Methodology (lead); Software (lead);

Validation (equal); Visualization (lead); Writing – original draft (lead); Writing – review & editing (equal). **John Dean Rooney:** Conceptualization (equal); Data curation (supporting); Investigation (supporting); Methodology (supporting); Project administration (supporting); Software (supporting); Supervision (supporting); Validation (equal); Visualization (supporting); Writing – original draft (supporting); Writing – review & editing (equal). **Hongwen Jiang:** Conceptualization (equal); Data curation (supporting); Funding acquisition (lead); Investigation (supporting); Methodology (supporting); Project administration (supporting); Resources (equal); Supervision (lead); Validation (equal); Writing – review & editing (equal).

DATA AVAILABILITY

The data that support the findings of this study are available from the corresponding author upon reasonable request.

REFERENCES

[1]A. R. Mills, C. R. Guinn, M. J. Gullans, A. J. Sigillito, M. M. Feldman, E. Nielsen, and J. R. Petta, "Two-qubit silicon quantum processor with operation fidelity exceeding 99%," Sci. Adv. **8**, 5130 (2022).

[2]J. Yoneda, K. Takeda, T. Otsuka, T. Nakajima, M. R. Delbecq, G. Allison, T. Honda, T. Kodera, S. Oda, Y. Hoshi, N. Usami, K. M. Itoh, and S. Tarucha, "A quantum-dot spin qubit with coherence limited by charge noise and fidelity higher than 99.9%," Nat. Nanotechnol. **13**, 102–106 (2018).

[3]T. Hensgens, T. Fujita, L. Janssen, X. Li, C. J. V. Diepen, C. Reichl, W. Wegscheider, S. D. Sarma, and L. M. Vandersypen, "Quantum simulation of a Fermi-Hubbard model using a semiconductor quantum dot array," Nature **548**, 70–73 (2017).

[4]X. Wang, E. Khatami, F. Fei, J. Wyrick, P. Namboodiri, R. Kashid, A. F. Rigosi, G. Bryant, and R. Silver, "Experimental realization of an extended Fermi-Hubbard model using a 2D lattice of dopant-based quantum dots," Nat. Commun. **13**, 6824 (2022).

[5]L. DiCarlo, H. J. Lynch, A. C. Johnson, L. I. Childress, K. Crockett, C. M. Marcus, M. P. Hanson, and A. C. Gossard, "Differential charge sensing and charge delocalization in a tunable double quantum dot," Phys. Rev. Lett. **92**, 226801 (2004).

[6]D. Wei, H. O. Li, G. Cao, G. Luo, Z. X. Zheng, T. Tu, M. Xiao, G. C. Guo, H. W. Jiang, and G. P. Guo, "Tuning inter-dot tunnel coupling of an etched graphene double quantum dot by adjacent metal gates," Sci. Rep. **3**, 3175 (2013).

[7]C. B. Simmons, M. Thalakulam, B. M. Rosemeyer, B. J. V. Bael, E. K. Sackmann, D. E. Savage, M. G. Lagally, R. Joynt, M. Friesen, S. N. Coppersmith, and M. A. Eriksson, "Charge sensing and controllable tunnel coupling in a Si/SiGe double quantum dot," Nano Lett. **9**, 3234–3238 (2009).

[8]S. F. Neyens, E. R. MacQuarrie, J. P. Dodson, J. Corrigan, N. Holman, B. Thorgrimsson, M. Palma, T. McJunkin, L. F. Edge, M. Friesen, S. N. Coppersmith, and M. A. Eriksson, "Measurements of capacitive coupling within a quadruple-quantum-dot array," Phys. Rev. Appl. **12**, 064049 (2019).

[9]X. Wang, S. Yang, and S. D. Sarma, "Quantum theory of the charge-stability diagram of semiconductor double-quantum-dot systems," Phys. Rev. B: Condens. Matter Mater. Phys. **84**, 115301 (2011).

[10]S. Das Sarma, X. Wang, and S. Wang, "Hubbard model description of silicon spin qubits: Charge stability diagram and tunnel coupling in Si double quantum dots," Phys. Rev. B: Condens. Matter Mater. Phys. **83**, 235314 (2011).

[11]S. Yang, X. Wang, and S. D. Sarma, "Generic Hubbard model description of semiconductor quantum-dot spin qubits," Phys. Rev. B: Condens. Matter Mater. Phys. **83**, 161301(R) (2011).

[12]C. J. van Diepen, P. T. Eendebak, B. T. Buijtendorp, U. Mukhopadhyay, T. Fujita, C. Reichl, W. Wegscheider, and L. M. K. Vandersypen, "Automated tuning of inter-dot tunnel coupling in double quantum dots," Appl. Phys. Lett. **113**, 033101 (2018).

[13]M. Nurizzo, B. Jadot, P. A. Mortemousque, V. Thiney, E. Chanrion, M. Dartiailh, A. Ludwig, A. D. Wieck, C. Bäuerle, M. Urdampilleta, and T. Meunier, "Controlled quantum dot array segmentation via highly tunable interdot tunnel coupling," Appl. Phys. Lett. **121**, 084001 (2022).

[14]H. Liu, B. Wang, N. Wang, Z. Sun, H. Yin, H. Li, G. Cao, and G. Guo, "An automated approach for consecutive tuning of quantum dot arrays," Appl. Phys. Lett. **121**, 084002 (2022).

[15]S. K. Gorman, M. A. Broome, J. G. Keizer, T. F. Watson, S. J. Hile, W. J. Baker, and M. Y. Simmons, "Extracting inter-dot tunnel couplings between few donor quantum dots in silicon," New J. Phys. **18**, 053041 (2016).

[16]T. Botzem, M. D. Shulman, S. Foletti, S. P. Harvey, O. E. Dial, P. Bethke, P. Cerfontaine, R. P. McNeil, D. Mahalu, V. Umansky, A. Ludwig, A. Wieck, D. Schuh, D. Bougeard, A. Yacoby, and H. Bluhm, "Tuning methods for semiconductor spin qubits," Phys. Rev. Appl. **10**, 054026 (2018).

[17]J. D. Teske, S. S. Humpohl, R. Otten, P. Bethke, P. Cerfontaine, J. Dedden, A. Ludwig, A. D. Wieck, and H. Bluhm, "A machine learning approach for automated fine-tuning of semiconductor spin qubits," Appl. Phys. Lett. **114**, 133102 (2019).

[18]R. Durrer, B. Kratochwil, J. V. Koski, A. J. Landig, C. Reichl, W. Wegscheider, T. Ihn, and E. Greplova, "Automated tuning of double quantum dots into specific charge states using neural networks," Phys. Rev. Appl. **13**, 054019 (2020).

[19]J. Darulová, S. J. Pauka, N. Wiebe, K. W. Chan, G. C. Gardener, M. J. Manfra, M. C. Cassidy, and M. Troyer, "Autonomous Tuning and Charge-State Detection of Gate-Defined Quantum Dots," Phys. Rev. Appl. **13**, 054005 (2020).

[20]J. P. Zwolak, T. Mcjunkin, S. S. Kalantre, S. S. Kalantre, J. P. Dodson, E. R. Macquarrie, D. E. Savage, M. G. Lagally, S. N. Coppersmith, S. N. Coppersmith, M. A. Eriksson, J. M. Taylor, J. M. Taylor, and J. M. Taylor, "Autotuning of double-dot devices in situ with machine learning," Phys. Rev. Appl. **13**, 034075 (2020).

[21]L. Szulakowska and J. Dai, "Bayesian autotuning of Hubbard model quantum simulators," http://arxiv.org/abs/2210.03077 (2022).

[22]T. A. Baart, P. T. Eendebak, C. Reichl, W. Wegscheider, and L. M. Vandersypen, "Computer-automated tuning of semiconductor double quantum dots into the single-electron regime," Appl. Phys. Lett. **108**, 213104 (2016).

[23]A. R. Mills, M. M. Feldman, C. Monical, P. J. Lewis, K. W. Larson, A. M. Mounce, and J. R. Petta, "Computer-automated tuning procedures for semiconductor quantum dot arrays," Appl. Phys. Lett. **115**, 113501 (2019).

[24]T. K. Hsiao, C. J. V. Diepen, U. Mukhopadhyay, C. Reichl, W. Wegscheider, and L. M. Vandersypen, "Efficient orthogonal control of tunnel couplings in a quantum dot array," Phys. Rev. Appl. **13**, 054018 (2020).

[25]S. S. Kalantre, J. P. Zwolak, S. Ragole, X. Wu, N. M. Zimmerman, M. D. Stewart, and J. M. Taylor, "Machine learning techniques for state recognition and auto-tuning in quantum dots," npj Quantum Inf. **5**, 6 (2019).

[26]J. P. Zwolak, S. S. Kalantre, X. Wu, S. Ragole, and J. M. Taylor, "Qflow lite dataset: A machine-learning approach to the charge states in quantum dot experiments," PLoS One **13**, e0205844 (2018).

[27]N. M. van Esbroeck, D. T. Lennon, H. Moon, V. Nguyen, F. Vigneau, L. C. Camenzind, L. Yu, D. M. Zumbühl, G. A. D. Briggs, D. Sejdinovic, and N. Ares, "Quantum device fine-tuning using unsupervised embedding learning," New J. Phys. **22**, 095003 (2020).

[28]J. P. Zwolak, T. McJunkin, S. S. Kalantre, S. F. Neyens, E. R. MacQuarrie, M. A. Eriksson, and J. M. Taylor, "Ray-based framework for state identification in quantum dot devices," PRX Quantum **2**, 020335 (2021).

[29]J. Ziegler, T. McJunkin, E. S. Joseph, S. S. Kalantre, B. Harpt, D. E. Savage, M. G. Lagally, M. A. Eriksson, J. M. Taylor, and J. P. Zwolak, "Toward robust autotuning of noisy quantum dot devices," Phys. Rev. Appl. **17**, 024069 (2022).

[30]J. Ziegler, F. Luthi, M. Ramsey, F. Borjans, G. Zheng, and J. P. Zwolak, "Tuning arrays with rays: Physics-informed tuning of quantum dot charge states," Phys. Rev. Appl. **20**, 034067 (2023).

[31]J. Ziegler, F. Luthi, M. Ramsey, F. Borjans, G. Zheng, and J. P. Zwolak, "Automated extraction of capacitive coupling for quantum dot systems," Phys. Rev. Appl. **19**, 054077 (2023).
[32]W. G. V. D. Wiel, S. D. Franceschi, J. M. Elzerman, T. Fujisawa, S. Tarucha, and L. P. Kouwenhoven, "Electron transport through double quantum dots," Rev. Mod. Phys. **75**, 1–22 (2002).
[33]C. Volk, A. M. Zwerver, U. Mukhopadhyay, P. T. Eendebak, C. J. van Diepen, J. P. Dehollain, T. Hensgens, T. Fujita, C. Reichl, W. Wegscheider, and L. M. Vandersypen, "Loading a quantum-dot based "qubyte" register," npj Quantum Inf. **5**, 29 (2019).
[34]A. Secchi and F. Troiani, "Multi-dimensional quantum capacitance of the two-site Hubbard model: The role of tunable interdot tunneling," Entropy **25**, 82 (2023).